LETTER

doi:10.1038/nature25505

Pulsating aurora from electron scattering by chorus waves

S. Kasahara[1], Y. Miyoshi[2], S. Yokota[3], T. Mitani[4], Y. Kasahara[5], S. Matsuda[2], A. Kumamoto[6], A. Matsuoka[4], Y. Kazama[7], H. U. Frey[8], V. Angelopoulos[9], S. Kurita[2], K. Keika[1], K. Seki[1] & I. Shinohara[4]

Auroral substorms, dynamic phenomena that occur in the upper atmosphere at night, are caused by global reconfiguration of the magnetosphere, which releases stored solar wind energy[1,2]. These storms are characterized by auroral brightening from dusk to midnight, followed by violent motions of distinct auroral arcs that suddenly break up, and the subsequent emergence of diffuse, pulsating auroral patches at dawn[1,3]. Pulsating aurorae, which are quasiperiodic, blinking patches of light tens to hundreds of kilometres across, appear at altitudes of about 100 kilometres in the high-latitude regions of both hemispheres, and multiple patches often cover the entire sky. This auroral pulsation, with periods of several to tens of seconds, is generated by the intermittent precipitation of energetic electrons (several to tens of kiloelectronvolts) arriving from the magnetosphere and colliding with the atoms and molecules of the upper atmosphere[4–7]. A possible cause of this precipitation is the interaction between magnetospheric electrons and electromagnetic waves called whistler-mode chorus waves[8–11]. However, no direct observational evidence of this interaction has been obtained so far[12]. Here we report that energetic electrons are scattered by chorus waves, resulting in their precipitation. Our observations were made in March 2017 with a magnetospheric spacecraft equipped with a high-angular-resolution electron sensor and electromagnetic field instruments. The measured[13,14] quasiperiodic precipitating electron flux was sufficiently intense to generate a pulsating aurora, which was indeed simultaneously observed by a ground auroral imager.

Theories and computer simulations have provided a promising explanation for the origin of electron precipitation: the interaction between electrons and whistler-mode chorus waves near the magnetospheric equator[7,8,15,16]. After chorus waves are generated at the equator, they propagate towards higher latitudes (grey wavy arrows in Fig. 1) and interact with bouncing, counter-streaming electrons in both hemispheres. As these electrons are scattered by the Lorentz force of the chorus waves, some of them become nearly aligned with the field, fall into the empty electron loss cone (blue open arrow in Fig. 1a), fill it (blue filled arrows in Fig. 1a), and precipitate into the upper atmosphere (top left in Fig. 1a).

Data from the THEMIS (Time History of Events and Macroscale Interactions during Substorms) spacecraft and ground-based imagers have shown a correlation between chorus-wave modulation and auroral patch pulsation[9,10]. Geosynchronous satellite measurements have revealed a correlation between electron flux modulation and auroral pulsation[17]. However, direct evidence of interaction between chorus waves and precipitating electrons at the source region—the connection needed to verify the whistler-mode chorus–electron interaction theory of pulsating aurorae—has not been obtained. This is principally because of the large acceptance angle of earlier space plasma instruments, which prohibited them from distinguishing small loss cones in the equatorial magnetosphere. Thus, it has been difficult to directly establish the association between precipitating electrons hidden inside loss cones and the chorus waves. The high angular resolution of our instrumentation has enabled us to overcome this limitation.

On 2017 March 27, auroral pulsations were observed by the ground-based auroral All-Sky Imagers (ASIs) of the THEMIS mission[18] (Fig. 2) when a magnetic storm with auroral substorm characteristics developed. Auroral snapshots illustrate the appearance and disappearance of pulsating auroral patches. The ionospheric footprint of the Exploration of energization and Radiation in Geospace (ERG, also called Arase) spacecraft[13,14], which was launched in December 2016 and started observations in March 2017, was traced with an empirical magnetic field model[19] and plotted over the auroral images (red crosses in Fig. 2). The model footprint is well within the fields of view of the ASIs in which the auroral pulsations can be clearly detected (see also Supplementary Video 1). Depending on the instantaneous magnetospheric configuration, however, the actual footprint may be displaced from the model by a few degrees in magnetic latitude and longitude[20] (fewer than several hundred kilometres in both directions). Therefore, the model footprint should be regarded as approximately located in a wide area where pulsating aurorae were observed (we note that the field of view of an ASI is about 1,000 km across, larger than the mapping uncertainties). Electrons with sufficient energy flux to cause a visible aurora were observed near the equator, closely correlated with chorus waves when the footprint of ERG was located in a region replete with pulsating auroral patches.

During morning hours in magnetic local time, ERG captured a correlation between wave activity and particle flux modulations near the magnetospheric equator. During the 30-min duration of the observation near the equator, waves are seen intermittently in the power spectra of the magnetic (Fig. 3a) and electric fields (Extended Data Fig. 1a) in both the lower-band ($<0.5f_{ce}$) and upper-band ($>0.5f_{ce}$) frequency ranges (where f_{ce} is the electron gyrofrequency). Despite dynamic chorus wave activity, northward-streaming electron fluxes outside the loss cone (with pitch angle, the angle between the particle velocity and the local magnetic field, from 20° to 40°) are relatively stable and do not show any apparent correlation with the waves (Fig. 3c). This is consistent with the absence of correlation between electron flux and chorus waves in previous observations.

Dramatic modulations of the electron flux in concert with chorus waves do occur in the loss cone, however. The northward loss-cone electron flux (Fig. 3b), as measured by the Medium-Energy Particle experiments – electron analyser (MEP-e) onboard ERG with a

[1]Department of Earth and Planetary Science, School of Science, University of Tokyo, 7-3-1 Hongo, Bunkyo-ku, Tokyo, Japan. [2]Institute for Space-Earth Environmental Research, Nagoya University, Furo-cho, Chikusa-ku, 24105 Nagoya, Aichi, Japan. [3]Department of Earth and Space Science, Graduate School of Science, Osaka University, 1-1 Machikaneyama-cho, Toyonaka, Osaka, Japan. [4]Institute of Space and Astronautical Science, 3-1-1 Yoshinodai, Chuo-ku, Sagamihara, Kanagawa, Japan. [5]Graduate School of Natural Science and Technology, Kanazawa University, Kakuma-machi, Kanazawa, Ishikawa, Japan. [6]Graduate School of Science, Tohoku University, 6-3 Aoba, Aramaki, Aoba-ku, Sendai 980-8578 Japan. [7]Academia Sinica Institute of Astronomy and Astrophysics, 11F Astronomy-Mathematics Building, AS/NTU, No. 1, Sec. 4, Roosevelt Road, Taipei 10617, Taiwan. [8]Space Sciences Laboratory, University of California, Berkeley, California 94720-7450, USA. [9]Department of Earth, Planetary and Space Sciences, University of California, Los Angeles, California 90095-1567, USA.

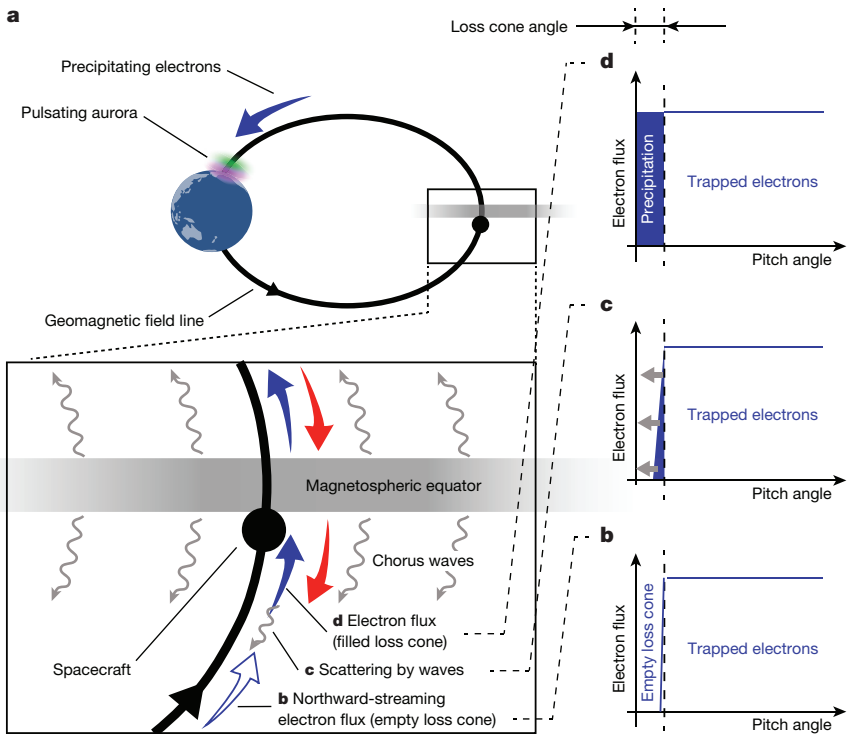

Figure 1 | Schematic of electron scattering by chorus waves, resulting in a pulsating aurora. a, The open blue arrow represents northward-streaming electrons with an empty loss cone (**b**) before chorus waves interact with them (**c**). The blue filled arrows represent the same electrons but with a filled loss cone (**d**) after their interaction with chorus waves (pitch-angle scattering by waves). The red arrows represent loss-cone-filling electrons streaming southwards. The spacecraft location is denoted by a black filled circle. **b**–**d**, The evolution of the electron PAD. Because chorus activity is intermittent, loss cone filling and depletion are repeated, causing auroral pulsations.

3.5° field of view (full-width at half-maximum), shows repeated enhancements and depletions over a broad energy range from 10 keV to 30 keV, in striking correspondence with bursts of lower-band chorus waves (Fig. 3a).

The correlation between chorus waves and loss-cone electron flux is more clearly presented in Fig. 4, which focuses on the flux of 24.5-keV electrons (selected because of the good loss-cone coverage) and a magnetic wave power spectral density of 0.38–0.64 kHz. This combination of energy and frequency satisfies the cyclotron resonance condition[21] (thus enabling considerable electron scattering) if we assume an electron density of 3 cm^{-3}, which is typical of this region[22], and it is also consistent with the observed frequency of the faint signature of an upper hybrid resonance wave (Extended Data Fig. 1a). The excellent correlation between loss-cone electrons (black solid lines in Fig. 4) and chorus waves (blue dash-dotted lines in Fig. 4) indicates that wave–particle interaction is indeed taking place. Upon close examination of Fig. 4, we see that the loss-cone flux is strongly modulated on a timescale of 10 s (or less, although the time resolution of the loss-cone measurement is 8 s, and thus shorter periods cannot be resolved), within the typical range of auroral pulsations. As expected from low-altitude observations[5,11], the flux is modulated by a factor of 2 to 3. Furthermore, when the loss cone is filled, the measured electron energy flux in the atmosphere is sufficient to excite visible aurorae. Specifically, it is several times 10^9 keV $cm^{-2}\,s^{-1}$ or several erg $cm^{-2}\,s^{-1}$—comparable to, but above, the threshold for visible aurorae[23] (Extended Data Fig. 2 further illustrates the correlation between auroral patch pulsation and the loss-cone electron flux, as well as the chorus waves).

Figure 4 also illustrates that the variability in the quasiparallel flux outside the loss cone (shown by black dashed lines) is nearly stable compared to the dynamic modulation of the loss-cone flux and chorus wave power. This indicates that the observed electron flux just outside the loss cone does not provide clear evidence of precipitation, which explains why previous measurements did not reveal the wave–particle correlation that causes pulsating aurorae.

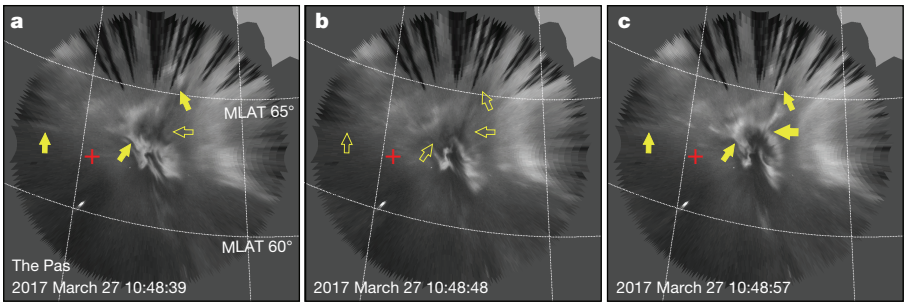

Figure 2 | Auroral snapshots around the footprint of ERG. Successive clear-sky images (10:48:39 to10:48:57 UT) from a ground station (the Pas). Distinct pulsating patches in the field of view of the Pas are indicated by yellow arrows. The filled and open arrows correspond to pulsations that are 'on' (bright aurora) or 'off' (no aurora), respectively. The red crosses show the nominal spacecraft footprint. The dotted lines illustrate magnetic coordinates every 5° in latitude and 15° in longitude, respectively. Supplementary Video 1 shows the full motion of the pulsating auroral patches in a 3-s cadence. MLAT, magnetic latitude.

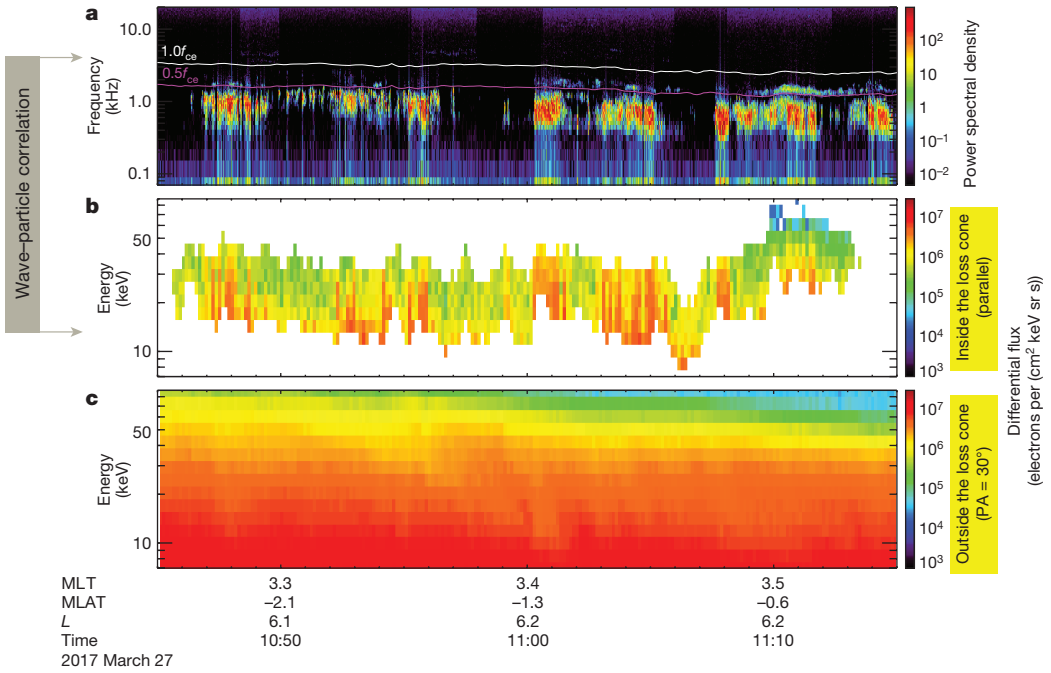

Figure 3 | *In situ* observations by ERG. a, Frequency–time spectrogram of the magnetic field power spectral density (in square picoteslas per hertz), showing chorus waves. The magenta and white lines indicate $0.5f_{ce}$ and $1.0f_{ce}$, respectively, relative to the local magnetic field. **b**, **c**, Energy–time spectrograms for differential fluxes of electrons (expressed in electrons per (cm^2 keV sr s)) in the loss cone (pitch angles PA < 2°) (**b**) and outside the loss cone, but quasiparallel to the magnetic field (PA = 20°–40°) (**c**). In **b**, white areas indicate absence of loss-cone measurements owing to the instrument's limited field of view. MLT, magnetic local time of the spacecraft; *L*, distance (in Earth radii) where a magnetic field line passing through the spacecraft crosses the magnetospheric equator.

The interpretation of this observation is illustrated in Fig. 1 (bottom left box). The spacecraft was in the Southern Hemisphere but quite close to the magnetospheric equator. The loss cone of the northward-streaming electrons, which is empty during quiet periods, fills with scattered electrons as southward-propagating chorus waves emerge. The evolution of the pitch-angle distribution (PAD) of the northward-streaming electron flux is schematically shown in the right panels of Fig. 1b–d. On the other hand, the electron flux in the southward-streaming loss cone (red arrows) is also seen in the observation (Extended Data Fig. 1d). Although this flux is also modulated (that is, varies with time), the correlation with the chorus waves is apparently weaker than that of the northward loss-cone flux (Fig. 3b and Extended Data Fig. 1c). For example, chorus waves were absent from 10:56 to 11:00 universal time (UT), while the southward-streaming loss cone continued to be filled. This can be expected because southward-streaming electrons must interact with northward-propagating chorus waves (presumably present in the Northern Hemisphere), which are not necessarily symmetrical with southward-propagating chorus waves.

We determined the location and physical mechanism of electron scattering into the loss cone and subsequent precipitation of energetic

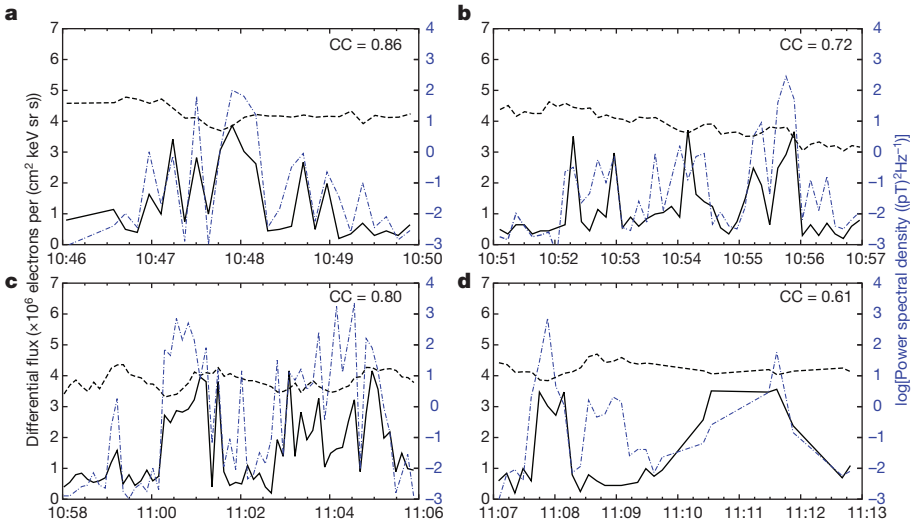

Figure 4 | Correlations between electron flux and wave power spectral density. The black solid line shows the modulation of the loss-cone electron flux (PA < 2°); the black dashed line indicates the nearly stable electron flux outside the loss cone (PA = 20°–40°). The blue dashed-dotted line shows the wave magnetic field power spectral density. The electron energy is 24.5 keV. The frequencies of the power spectral density are 0.64 kHz for **a**–**c** and 0.38 kHz for **d**, selected according to the resonance condition. The correlation coefficients (CC) between the loss-cone differential flux and the logarithmic power spectral density are shown.

electrons, which results in a pulsating aurora. Whether these results can be generalized across radial distances from Earth, different local times and geomagnetic activity conditions is yet to be determined. Comparing loss-cone fluxes with other potential scattering mechanisms, such as electrostatic electron cyclotron harmonic waves[7] and large-amplitude parallel electric fields[12], for which the correlated energy range is typically lower than that discussed here, would help to determine whether other wave types make a similar contribution to scattering. The physical process presented here should apply to the aurorae of Jupiter and Saturn, where chorus waves have been detected[24,25], and may also operate at other magnetized astrophysical objects.

Online Content Methods, along with any additional Extended Data display items and Source Data, are available in the online version of the paper; references unique to these sections appear only in the online paper.

Received 19 September; accepted 21 December 2017.

1. Akasofu, S. I. *Polar and Magnetospheric Substorms* 22–31, 222–224 (Springer, 1968).
2. Angelopoulos, V. *et al.* Tail reconnection triggering substorm onset. *Science* **321,** 931–935 (2008).
3. Duthie, D. D. & Scourfield, M. W. J. Aurorae and closed magnetic field lines. *J. Atmos. Terr. Phys.* **39,** 1429–1434 (1977).
4. Johnstone, A. D. Pulsating aurora. *Nature* **274,** 119–126 (1978).
5. McEwen, D. J. & Duncan, C. N. A campaign to study pulsating auroras. *Can. J. Phys.* **59,** 1029–1033 (1981).
6. Lessard, M. R. in *Auroral Phenomenology and Magnetospheric Processes: Earth And Other Planets* (eds Keiling, A. *et al.*) 55–68 (American Geophysical Union, 2012).
7. Ni, B. *et al.* Origins of the Earth's diffuse auroral precipitation. *Space Sci. Rev.* **200,** 205–259 (2016).
8. Thorne, R. M., Ni, B., Tao, X., Horne, R. B. & Meredith, N. P. Scattering by chorus waves as the dominant cause of diffuse auroral precipitation. *Nature* **467,** 943–946 (2010).
9. Nishimura, Y. *et al.* Identifying the driver of pulsating aurora. *Science* **330,** 81–84 (2010).
10. Nishimura, Y. *et al.* Multievent study of the correlation between pulsating aurora and whistler mode chorus emissions. *J. Geophys. Res.* **116,** A11221 (2011).
11. Miyoshi, Y. *et al.* Relation between fine structure of energy spectra for pulsating aurora electrons and frequency spectra of whistler mode chorus waves. *J. Geophys. Res. Space Phys.* **120,** 7728–7736 (2015).
12. Mozer, F. S., Agapitov, O. V., Hull, A., Lejosne, S. & Vasko, I. Y. Pulsating auroras produced by interactions of electrons and time domain structures. *J. Geophys. Res. Space Phys.* **122,** 8604–8616 (2017).
13. Miyoshi, Y. *et al.* in *Dynamics of the Earth's Radiation Belts and Inner Magnetosphere* (eds Summers, D. *et al.*) 103–116 (American Geophysical Union, 2012).
14. Miyoshi, Y. *et al.* Geospace exploration project: Arase (ERG). *J. Phys. Conf. Ser.* **869,** 012095 (2017).
15. Kennel, C. F. & Petschek, H. E. Limit on stably trapped particle fluxes. *J. Geophys. Res.* **71,** 1–28 (1966).
16. Trakhtengerts, V. Yu., Tagirov, V. R. & Chernous, S. A. A circulating cyclotron maser and pulsed VLF emissions. *Geomagn. Aeron.* **26,** 77–82 (1986).
17. Jaynes, A. N. *et al.* Pulsating auroral electron flux modulations in the equatorial magnetosphere. *J. Geophys. Res. Space Phys.* **118,** 4884–4894 (2013).
18. Mende, S. *et al.* The THEMIS array of ground-based observatories for the study of auroral substorms. *Space Sci. Rev.* **141,** 357–387 (2008).
19. Tsyganenko, N. A. & Sitnov, M. I. Modeling the dynamics of the inner magnetosphere during strong geomagnetic storms. *J. Geophys. Res.* **110,** A03208 (2005).
20. Nishimura, Y. *et al.* Estimation of magnetic field mapping accuracy using the pulsating aurora-chorus connection. *Geophys. Res. Lett.* **38,** L14110 (2011).
21. Horne, R. B. & Thorne, R. M. Potential waves for relativistic electron scattering and stochastic acceleration during magnetic storms. *Geophys. Res. Lett.* **25,** 3011–3014 (1998).
22. Sheeley, B. W., Moldwin, M. B., Rassoul, H. K. & Anderson, R. R. An empirical plasmasphere and trough density model: CRRES observations. *J. Geophys. Res.* **106,** 25631–25641 (2001).
23. Yahnin, A. G., Sergeev, V. A., Gvozdevsky, B. B. & Vennerstrom, S. Magnetospheric source region of discrete auroras inferred from their relationship with isotropy boundaries of energetic particles. *Ann. Geophys.* **15,** 943–958 (1997).
24. Katoh, Y. *et al.* Whistler mode chorus enhancements in association with energetic electron signatures in the Jovian magnetosphere. *J. Geophys. Res.* **116,** A02215 (2011).
25. Menietti, J. D. *et al.* Saturn chorus intensity variations. *J. Geophys. Res. Space Phys.* **118,** 5592–5602 (2013).

Supplementary Information is available in the online version of the paper.

Acknowledgements The observations presented here were obtained with the help of Mitsubishi Heavy Industries, Ltd, Meisei Electric Co., Ltd, Hamamatsu Photonics Co. Ltd, YS DESIGN Co., Ltd, NIPPI Co. Ltd, Sumitomo Heavy Industries, Ltd and TIERRA TECNICA Co. Ltd. We acknowledge the work of the members of the ERG project team over several years. Y.M. is supported by JSPS Kakenhi (15H05747, 15H05815 and 16H06286). Y. Kasahara is supported by JSPS Kakenhi (16H04056 and 16H01172). H.U.F. is supported by grant AGS-1004736 from the National Science Foundation (NSF) of the USA. I.S. is supported by JSPS Kakenhi (17H06140). We thank NASA for contract NAS5-02099, S. Mende and E. Donovan for use of the ASI data, the Canadian Space Agency for logistical support in fielding and data retrieval from the ground-based observatory stations, and the NSF for support of the Ground-based Imager and Magnetometer Network for Auroral Studies programme through grant AGS-1004736. The ERG (Arase) satellite science data is available from the ERG Science Centre operated by the Institute of Space and Astronautical Science of the Japan Aerospace eXploration Agency and the Institute for Space–Earth Environmental Research of Nagoya University (https://ergsc.isee.nagoya-u.ac.jp/index.shtml.en). We are grateful to J. Hohl for assistance in editing the manuscript. We also thank N. Umemura for assistance in source data archiving. S. Kasahara thanks T. Mukai and M. Fujimoto for discussions.

Author Contributions S. Kasahara developed the MEP-e instrument used in this study with S.Y. and T.M., identified the event, analysed the combined dataset and wrote the paper. Y.M. oversaw the production of the combined dataset and discussed its interpretation. Y. Kasahara, S.M. and A.K. provided Plasma Wave Experiment data and discussed the interpretation. A.M. provided MaGnetic Field experiment data. Y. Kazama assisted in the evaluation of MEP-e data through comparison with the Low-Energy Particle experiments – electron analyser. H.U.F. and V.A. provided ASI/THEMIS data and discussed the event and presentation of the results. S. Kurita evaluated the spacecraft footprint with Y.M. and discussed the event. K.K. and K.S. discussed the event and presentation. I.S. oversaw the ERG project and discussed the interpretation of the event. All authors reviewed the manuscript.

Author Information Reprints and permissions information is available at www.nature.com/reprints. The authors declare no competing financial interests. Readers are welcome to comment on the online version of the paper. Publisher's note: Springer Nature remains neutral with regard to jurisdictional claims in published maps and institutional affiliations. Correspondence and requests for materials should be addressed to S. Kasahara (s.kasahara@eps.s.u-tokyo.ac.jp).

METHODS

Electron analyser. The key observation in our dataset is the electron measurement made by the MEP-e sensor onboard the ERG spacecraft. The sensor comprises an electrostatic analyser (ESA) specifically designed for energetic particles[26] and avalanche photodiodes[27] (APDs). The ESA is an energy filter covering 7–87 keV with an energy resolution of 8%. The angular resolution is determined by combining the focusing property of the ESA with the size of the detector (or the APD). The ESA has a disk-like, 2π-rad field of view divided into 16 narrow elements, each of which corresponds to an APD. Using the spacecraft's spin motion, a full solid angle is swept (with certain dead angles due to gaps between detectors). Depending on the geometry (more specifically, the angle between the spacecraft's spin axis and the magnetic field), MEP-e may see the magnetic field direction (and thus observe the loss cone) once or twice in one spacecraft spin, as in the presented case. The sensor may also miss the magnetic field directions (the magnetic field direction drops at the gaps) or the loss cone may be observed for a longer time (if the spin axis is along the magnetic field direction). Neither of these scenarios occurred in the time period reported here.

Angular resolution. The most important property of the MEP-e sensor for this study—the angular resolution in two orthogonal directions—is shown in Extended Data Fig. 3. These calibration data were obtained by pre-flight laboratory experiments. Profiles are essentially the same for all 16 channels. Here the data are modelled with a Gaussian shape and a full-width at half-maximum of 3.5° for use in the evaluation of the loss-cone determination discussed below.

Loss cone determination. In Figs 3b and 4, as well as in Extended Data Fig. 1c and d, we have plotted the loss-cone electron flux. In these analyses, we used the following criterion for loss-cone measurements: when the angle between the centre of the field of view of the MEP-e and the magnetic field is smaller than 2°, the detected electrons are inside the loss cone. This approach needs caution regarding contamination from electrons outside the loss cone, because a fraction of the field of view can extend outside the loss cone. We carefully evaluated this effect (Extended Data Fig. 4) and found it to be insignificant (although not negligible), confirming the robustness of our analyses.

Estimation of precipitating electron energy flux. The downward electron energy flux F at the ionosphere, which contributes to the auroral illumination, is estimated as $F \approx (B_i/B_{eq})\, E\, J_{eq}\, \Delta\Omega\, \Delta E$, where the parameters are the magnetic field strength at the ionosphere ($B_i \approx 55{,}000$ nT) and at the equator (B_{eq}), the electrons' characteristic energy (E), the differential flux at the equator (J_{eq}), the solid angle of the loss cone ($\Delta\Omega$) and the energy range of the precipitating electrons (ΔE). On the basis of our *in situ* observation, we take $B_{eq} \approx 100$ nT, $E \approx 20$ keV, $J_{eq} \approx 4\times10^{6}$ keV cm^{-2} sr^{-1} s^{-1} keV^{-1} (here we take the peak value), $\Delta\Omega \approx 6\times10^{-3}$ sr and $\Delta E \approx 20$ keV to obtain a downward electron energy flux of about 5×10^{9} keV cm^{-2} s^{-1}, or 8 erg cm^{-2} s^{-1}.

Data availability. The ERG data presented here are publicly available from the ERG science centre website (https://ergsc.isee.nagoya-u.ac.jp/dataset/2017.l-1001.shtml.en). THEMIS-ASI data that support the findings of this study are publicly available at http://themis.ssl.berkeley.edu/data_all.shtml.

Code availability. The software used to read and analyse the data, part of the publicly available SPEDAS software package, is available at http://themis.ssl.berkeley.edu/software.shtml and can be used without any restrictions. All data have a common data file format (https://cdf.gsfc.nasa.gov/).

26. Kasahara, S. *et al.* Cusp type electrostatic analyzer for measurements of medium energy charged particles. *Rev. Sci. Instrum.* **77,** 123303 (2006).
27. Kasahara, S., Takashima, T. & Hirahara, M. Variability of the minimum detectable energy of an APD as an electron detector. *Nucl. Instr. Meth. A* **664,** 282–288 (2012).

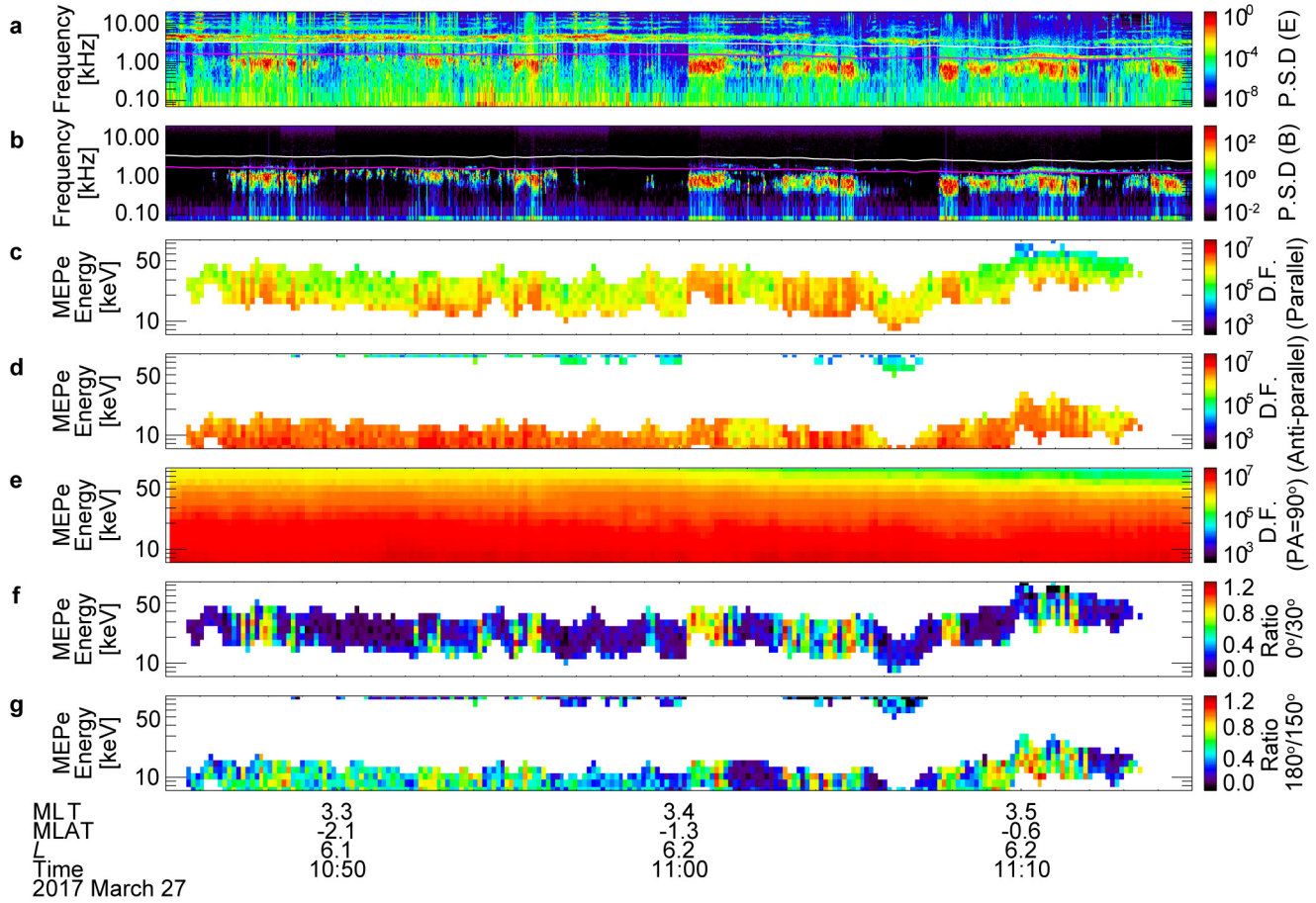

Extended Data Figure 1 | *In situ* observations by ERG with an additional dataset. a, **b**, Frequency–time spectrograms of the power spectral densities of the electric (**a**) and magnetic field (**b**), showing chorus waves. The magenta and white lines indicate $0.5f_{ce}$ and $1.0f_{ce}$, respectively, based on local magnetic field observations. **c**–**e**, Energy–time spectrograms for differential fluxes of loss-cone electrons parallel (pitch angles PA < 2°) (**c**) and anti-parallel (PA > 178°) (**d**) to the magnetic field and electrons perpendicular to the magnetic field (PA = 80°–100°) (**e**). Quasiparallel (PA = 20°–40°) and quasiantiparallel (PA = 140°–160°) electrons show essentially the same trend as that of the perpendicular flux. **f**, Flux(PA < 2°)/flux(PA = 20°–40°); **g**, flux(PA > 178°)/flux(PA = 140°–160°). The graphs in **b** and **c** are the same as those in Fig. 3a and b, respectively (but replotted here for comparison with **a** and **d**). The faint signature of an upper hybrid resonance wave at 12–16 kHz in **a** at about 11:10 UT is consistent with the assumed density of approximately 3 cm^{-3}.

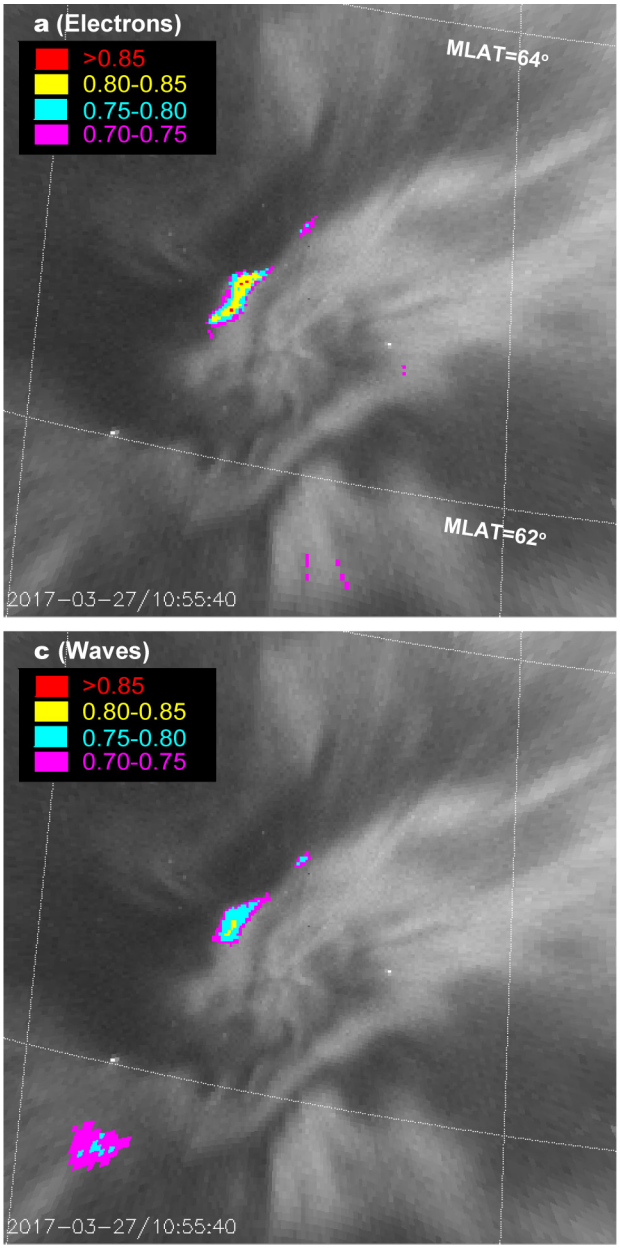

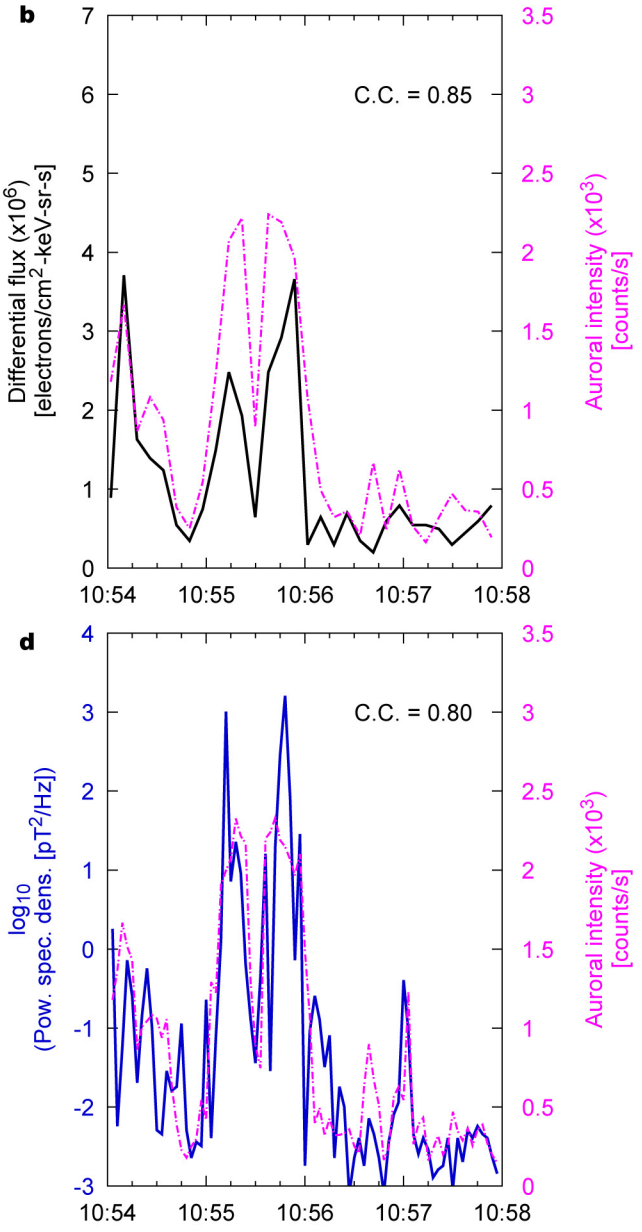

Extended Data Figure 2 | Correlation coefficients for auroral intensity. **a**, The colours (red, yellow, cyan and magenta) show the correlation coefficients between the auroral intensity and the loss-cone electron flux. **b**, Time series data of the loss-cone electron flux and the auroral intensity at a pixel at which electrons and chorus waves have nearly the highest correlation. The auroral intensity is plotted at the same time resolution as the electrons (about 8 s). **c**, **d**, The same as **a** and **b**, but for the chorus wave intensity. The wave intensity in **d** is plotted at the same time resolution as the auroral intensity (3 s). In **a** and **c**, the background auroral images are magnified around the centre of the field of view of the Pas station. Highest-correlation pixels are consistently located near the centre of both panels, suggesting the spacecraft footprint. The dashed lines in **a** and **c** illustrate magnetic coordinates every 2° in latitude and 5° in longitude. The displacement of the model footprint from the high-correlation pixels is approximately −0.5° and −5° in latitude and longitude, respectively, consistent with typical modelling errors[20]. Cross-correlations were calculated for the period 10:54:00–10:58:00 UT. In other time periods, high-correlation pixels were not commonly obtained, perhaps because of the fine structures of pulsating patches and the equatorial modulation regions near the spacecraft. For example, if the spacecraft leaves the localized modulation region as a result of magnetospheric configuration change, chorus waves and associated electron precipitation disappear at its location, but pulsating patches can continue to be 'on' if the equatorial modulation region still exists. In other words, although the spacecraft's footprint in the ionosphere can leave an illuminated patch owing to spatial reconfiguration of magnetic field line structures or plasma phenomena, the auroral intensity remains high at some pixels. Other reasons that make the above correlations difficult to identify, such as the contribution of soft electron (<10 keV) precipitation to higher-altitude (>100 km) illumination, may be studied in future work.

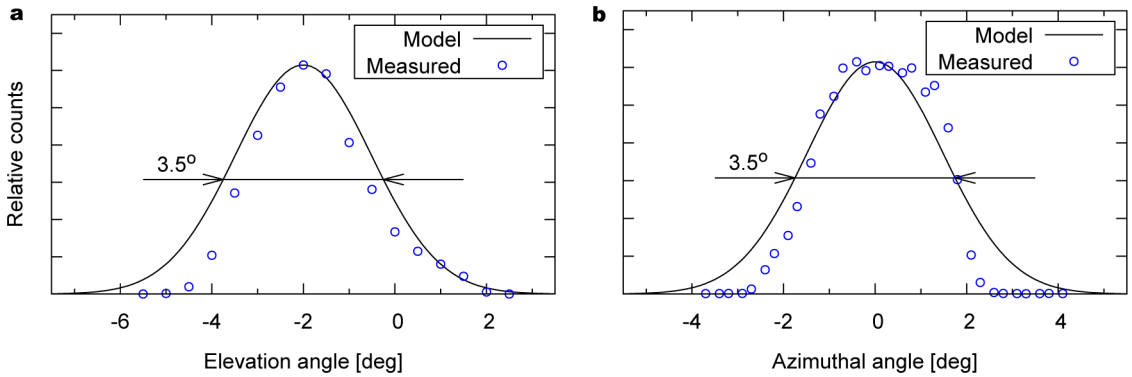

Extended Data Figure 3 | The angular response of MEP-e in two orthogonal directions. a, Sensor response as a function of elevation angle with respect to the sensor's mounting plane. **b**, Response in the sensor's azimuthal direction, which is orthogonal to the elevation angle. Blue circles, laboratory data; black line, Gaussian model. The model curves were used to obtain the analysis results shown in Extended Data Fig. 4. Profiles for one detector are shown here; similar profiles were obtained for the other 15 detectors.

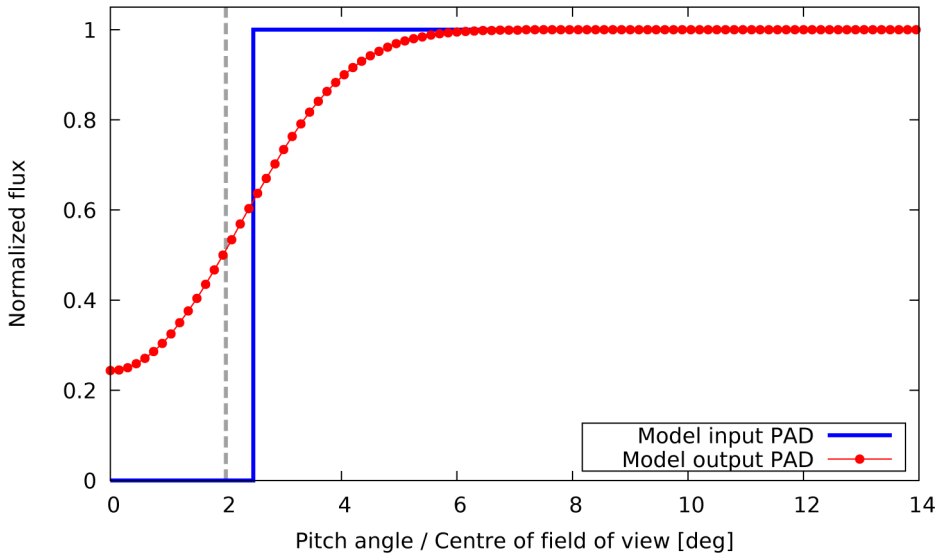

Extended Data Figure 4 | Results of PAD model taking the sensor's angular resolution into account. Because of the finite angular resolution, contamination from outside the loss cone cannot be completely negligible. The blue line indicates the model input PAD, which is isotropic except for the step-function drop at the loss-cone angle of 2.5° (the nominal loss-cone angle in the event presented in this paper, based on a local magnetic field of about 100 nT). The red curve shows how the electron PAD is modulated by the effect of the sensor's finite angular resolution. The grey dashed line indicates the threshold, 2°, for loss-cone selection (that is, if the angle between the centre of the field of view and the magnetic field is smaller than the threshold, the measured flux is considered to be the flux inside the loss cone). For this calculation, the sensor's field of view is modelled by a Gaussian cone (full-width at half-maximum, 3.5°), based on the ground calibration. For example, even when the middle of the sensor's field-of-view is centred along the magnetic field line and the actual electron PAD has an ideally empty loss cone, the instrument can inadvertently record about a few tens per cent of the flux from outside the loss cone. In our observations, however, the electron flux in the loss cone most often exhibits a filling ratio larger than 0.5, sometimes about 1, when the precipitation is 'on' (Fig. 4 and Extended Data Fig. 1f and g), too large to be explained by contamination alone. Also, synchronization with chorus waves cannot be produced by this instrumental effect.